

1 **Karst aquifer discharge response to rainfall interpreted as anomalous transport**

2 Dan Elhanati¹, Nadine Goeppert^{2, 3}, Brian Berkowitz¹

3

4 ¹Department of Earth and Planetary Sciences, Weizmann Institute of Science, Rehovot, Israel

5 ²Institute of Applied Geosciences, Division of Hydrogeology, Karlsruhe Institute of
6 Technology (KIT), Karlsruhe, Germany

7 ³Institute of Geological Sciences, Hydrogeology, Free University Berlin, Germany

8

9 Correspondence to: Dan Elhanati (dan.elhanati@gmail.com)

10

11

12

13 **Abstract**

14 The discharge measured in karst springs is known to exhibit distinctive long tails during
15 recession times following distinct discharge peaks of short duration. The long-tail behavior is
16 generally attributed to the occurrence of tortuous, ramified flow paths that develop in the
17 underground structure of karst systems. Modeling the discharge behavior poses unique
18 difficulties because of the poorly-delineated flow path geometry and generally scarce
19 information on the hydraulic properties of catchment-scale systems. In a different context,
20 modeling of long-tailed behavior has been addressed in studies of chemical transport. Here, an
21 adaptation of a continuous time random walk – particle tracking (CTRW-PT) framework for
22 anomalous transport is proposed, which offers a robust means to quantify long-tailed
23 breakthrough curves that often arise during chemical species transport under various flow
24 scenarios. A theoretical analogy is first established between partially water-saturated karst flow,
25 characterized by temporally varying water storage, and chemical transport involving
26 accumulation and release of a chemical tracer. This analogy is then used to develop and
27 implement a CTRW-PT model. Application of this numerical model to examination of three
28 years of summer rainfall and discharge data from a karst aquifer system – the Disnergshroef
29 high alpine site in the Austrian Alps – is shown to yield robust fits between modeled and
30 measured discharge values. In particular, the analysis underscores the predominance of slow
31 diffusive flow over rapid conduit flow. The study affirms the analogy between partially
32 saturated karst flow and chemical transport, exemplifying the compatibility of the CTRW-PT
33 model for this purpose. Within the specific context of the Disnergshroef karst system, these
34 findings highlight the predominance of slow diffusive flow over rapid conduit flow. The
35 agreement between measured and simulated data supports the proposed analogy between
36 partially saturated karst flow and chemical transport; it also highlights the potential ability of
37 the anomalous transport framework to further enhance modeling of flow and transport in karst
38 systems.

39 **1 Introduction**

40 Aquifers consist of various geological formations through which water can flow and carry
41 chemical species. The abundance of structural heterogeneities, ranging from intricate grain
42 arrangements at the pore scale to larger geologic structures and discontinuities at the meso- and
43 macroscopic scales, introduces irregular and tortuous flow paths that cannot be delineated
44 without a full physical description of the system. Achieving an accurate representation of flow
45 and transport therefore becomes increasingly difficult with an increase in the scale and
46 complexity of the groundwater system.

47 Karst systems, in particular, are known as structurally complex aquifers. They are composed
48 of many interconnected conduits, fractures and voids formed through the dissolution of soluble
49 rocks like limestone, dolostone and gypsum, which leads to the occurrence of multiple and
50 ramified flow paths (Bakalowicz, 2005). Karst terrains are usually described, in a vertical
51 cross-section, by distinct hydrological layers whose structure affect the response of the system
52 to incoming precipitation: (1) the surface soil layer; (2) the interface between the soil layer and
53 the deeper saturated zone (epikarst); and (3) the deep underground, mostly phreatic, zone
54 (endokarst). The soil and epikarst layers, known collectively as the exokarst, are known to
55 exhibit lateral flow of water above and below ground, until water reaches fractures or conduits
56 that allow them to flow rapidly to the endokarst. This allows for some water to infiltrate
57 downwards, while some may remain in the vadose zone and be subjected to both percolation
58 and evapotranspiration (Jukić and Denić-Jukić, 2009). The epikarst and endokarst layers each
59 consist of a primary (matrix) porosity composed of all bulk pores, a secondary porosity
60 composed of the smaller joints and fissure developed during diagenesis and/or by tectonic
61 processes, and a tertiary porosity of large fractures and voids (conduits) created due to
62 karstification (Ford and Williams, 2007). The different types of porosities usually exhibit
63 distinct flow patterns: rapid flow in the conduits and slow diffusive flow in the smaller fissures
64 and the matrix. The different karst layers may exhibit a changing role in facilitating the flow or
65 retention of water through the system as a function of water level or recharge intensity
66 (Hartmann et al., 2014). Furthermore, the connectivity of the different porosities often results
67 in a fracture-cave network, which dominates the flow structures in karst systems (Zhang et al.,
68 2022).

69 To date, various hydrological models have been developed specifically for karst systems, to
70 describe the commonly observed flow and transport patterns that are specific to karst systems.

71 In particular, distributed models rely on creating a grid of cells with different hydrological
72 parameters (e.g., Anderson & Radić, 2022; Chen et al., 2017; Kaufmann & Turk, 2016), while
73 lumped parameter models parameterize the characteristics of the system. Lumped parameter
74 models are based on different system conceptualizations (e.g., Chen and Goldscheider, 2014;
75 Cinkus et al., 2023b; Fleury et al., 2009; Jukić and Denić-Jukić, 2009; Mazzilli et al., 2019;
76 Rimmer and Salinger, 2006; Tritz et al., 2011), as well as neural network approaches (e.g.,
77 Afzaal et al., 2020; Cinkus et al., 2023b; Kratzert et al., 2018; Renard and Bertrand, 2017;
78 Wunsch et al., 2022). A common, significant feature encountered in karst systems – which is
79 difficult to capture in models – is the interplay of rapid and slow flow which manifests as long-
80 tailed measurements of both discharge rates (e.g., Frank et al., 2021) and chemical tracer
81 concentrations (e.g., Goepfert et al., 2020) observed at karst springs.

82 In many systems that exhibit highly variable spatial velocity distributions or temporal
83 behaviors, measurements of long tails in arrival times may be encountered. In the context of
84 chemical transport in porous media, long tails in the arrival time of chemical tracers have long
85 been a subject of study. Anomalous transport, which describes chemical transport that deviates
86 from the behavior described by the traditional Advection-Dispersion Equation (ADE), is
87 prevalent in many system and transport scenarios (Berkowitz et al., 2006); deviations from
88 solutions of traditional transport equations were observed even for non-dispersive diffusion
89 (Cortis and Knudby, 2006). It has been shown that higher subsurface heterogeneity increases
90 the degree of anomalous transport by inducing longer than expected (for Fickian transport)
91 arrival times (Edery et al., 2016, 2014). Traditional ADE based models, which rely on
92 averaging the physical traits of the medium into a single coefficient, do not accurately predict
93 transport in many cases. To correctly describe long-tailed events, various modeling approaches
94 have been developed. Among these, the Continuous Time Random Walk (CTRW) framework
95 has emerged as suitable for simulating diverse transport scenarios, including the behavior of a
96 long-time field-scale hydrological catchment (Dentz et al., 2023). The CTRW framework
97 accounts for anomalous transport behavior and offers a more physically realistic representation
98 of the transport processes that are encountered in real-world groundwater systems. The
99 framework defines waiting time and step length distributions that are applied in random walks
100 which are continuous in time, thereby capturing the complexity of transport processes
101 (Berkowitz et al., 2006).

102 In the current study, the CTRW framework, which has been developed to model anomalous
103 chemical transport, is utilized to quantify long-tailing of water flow in karst systems. In this

104 context, data from the Disnergshroef alpine study site in Vorarlberg, Austria are revisited
105 (Frank et al., 2021). This high-alpine karst system has been thoroughly studied and offers a
106 catchment with a well-defined spatial boundary. The surface of the karst system is composed
107 mainly of bare limestone with very limited soil coverage, resulting in negligible surface runoff.
108 The plateau is characterized by dolines and depressions, further facilitating the direct flow of
109 water into the subsurface. The vadose zone is estimated to be several hundred meters thick
110 (Frank et al., 2021). The known extent of its recharge basin and the corresponding single spring
111 which serves as its outlet allow for measurements of both recharge and discharge. Previous
112 studies (e.g., Frank et al., 2021) identified a distinct discharge response approximately 5.5
113 hours after a rainfall event, with variations in electrical conductivity, indicative of fresh rainfall
114 arriving at the spring outlet, observed ~8 hours post-event. While existing models provided a
115 good overall fit and illuminated the divide between epikarst-to-conduit and matrix-to-conduit
116 flows, they were less effective in matching the long tails.

117 Accurate modeling of water movement in these complex subsurface landscapes is crucial, as
118 many regions rely on karst systems for drinking water (Stevanović, 2019). Here, a theoretical
119 and practical development of the CTRW framework is proposed as an approach to simulate the
120 intricate dynamics of water movement in karst environments.

121 **2 Conceptual and mathematical development**

122 The conceptual development of the CTRW framework to model water flow in karst systems is
123 founded on a proposed ansatz, in which water flow is conceptualized as distinct “water parcels”
124 (i.e., infinitesimal volumes of water) that travel along the available flow paths. Local volumes
125 along the flow paths, e.g., caverns, conduits, and voids, allow for the accumulation and release
126 of water parcels, and define mobile and immobile zones for water flow. The ansatz asserts that
127 the accumulation and release of water parcels in the various volumes in the karst system
128 resemble the accumulation and release of “parcels” of a chemical tracer (i.e., infinitesimal
129 volumes of tracer) over time in a porous medium. As shown in Fig. 1, a cavern acting as a
130 storage region for water parcels is analogous to tracer parcels accumulating in an immobile (or
131 less mobile) zone. For both cases, it should be noted that local accumulation of water parcels
132 or increase in concentration of a chemical will increase their respective fluxes in the immediate
133 local vicinity. Under similar hydraulic conditions both fluxes create distinctive long tails when
134 measured over a control plane at the system outlet, which is primarily a result of the structural
135 heterogeneity of the system.

136 Characterizing the flow of water through an infinitesimal control volume can be formulated in
 137 terms of a mass balance equation that equates the net rate of fluid flow in the control volume
 138 to the time rate of change of fluid mass storage within it:

$$139 \quad -\frac{\partial(\rho q_x)}{\partial x} - \frac{\partial(\rho q_y)}{\partial y} - \frac{\partial(\rho q_z)}{\partial z} = \frac{\partial(\rho n)}{\partial t} \quad (1)$$

140 where n is porosity, ρ water density, and the three components of the specific discharge \mathbf{q} are
 141 described as q_x , q_y and q_z . This equation describes the mass balance in a fully saturated domain,
 142 in which the void volume (V_v) is completely filled with water ($V_w=V_v$). The moisture content
 143 ($\theta = \frac{V_w}{V_{tot}}$) in these cases is equal to the porosity, and the degree of saturation ($\theta' = \frac{\theta}{n}$) is equal
 144 to 1.

145 For partially saturated flow, the degree of saturation is less than 1 and the moisture content is
 146 smaller than n (as $V_w < V_v$). Adjusting the equation for partially saturated transient flow yields
 147 (allowing for water compressibility, to retain generality):

$$148 \quad -\frac{\partial(\rho q_x)}{\partial x} - \frac{\partial(\rho q_y)}{\partial y} - \frac{\partial(\rho q_z)}{\partial z} = \frac{\partial(\rho \theta' n)}{\partial t} . \quad (2)$$

149 Substituting $\theta = \theta' n$:

$$150 \quad -\frac{\partial(\rho q_x)}{\partial x} - \frac{\partial(\rho q_y)}{\partial y} - \frac{\partial(\rho q_z)}{\partial z} = \frac{\partial(\rho \theta)}{\partial t} . \quad (3)$$

151 Deriving a description for the transport of a chemical tracer in a fully saturated porous medium
 152 within a similar control volume is achieved by a mass balance equation:

$$153 \quad -\frac{\partial F_x}{\partial x} - \frac{\partial F_y}{\partial y} - \frac{\partial F_z}{\partial z} = n \frac{\partial C}{\partial t} . \quad (4)$$

154 The chemical mass flux (in one direction) is defined by advection and diffusion terms:

$$155 \quad F_i = q_i C - n D_i \frac{\partial C}{\partial i} . \quad (5)$$

156 Substituting (5) into (4) yields

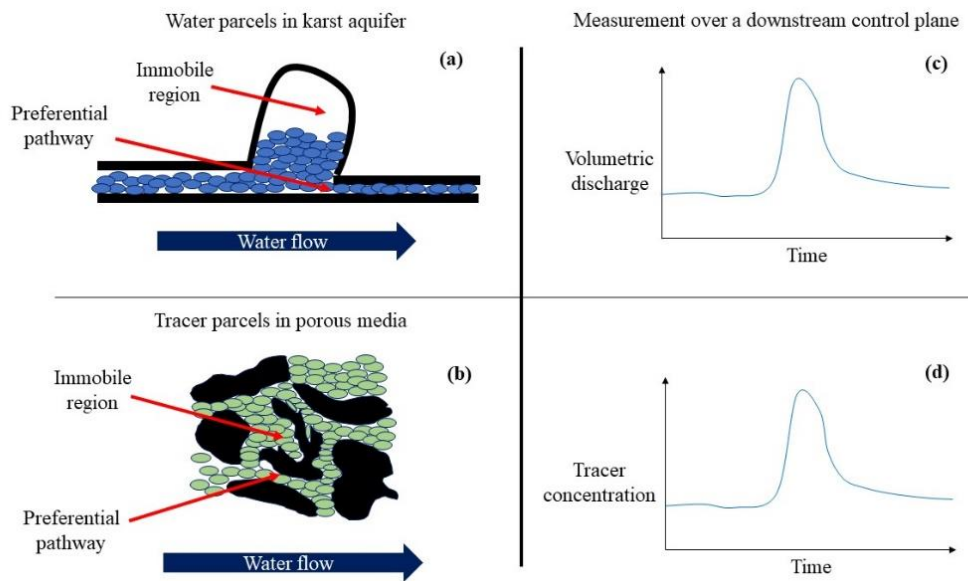
$$157 \quad \frac{\partial}{\partial x} \left(n D_x \frac{\partial C}{\partial x} \right) - \frac{\partial}{\partial x} (q_x C) + \frac{\partial}{\partial y} \left(n D_y \frac{\partial C}{\partial y} \right) - \frac{\partial}{\partial y} (q_y C) + \frac{\partial}{\partial z} \left(n D_z \frac{\partial C}{\partial z} \right) - \frac{\partial}{\partial z} (q_z C) = n \frac{\partial C}{\partial t} . \quad (6)$$

158 (Note that the appearance of the porosity variable, n , in the terms of Eqs. (4)-(6) is easily
 159 rearranged, and that these equations can be simplified if n is assumed constant in space.)

160 By drawing the analogy in the ansatz between the dynamics of water parcels and chemical
 161 tracers, and noting the similar forms of Eqs. (3) and (4), the description of the mass balance of
 162 water in a partially saturated domain is (at least) mathematically analogous to the description
 163 of the mass balance of a chemical tracer in a saturated domain. This results in the intrinsic
 164 connection of $C \Leftrightarrow \rho \theta$, both with units of mass per volume. In a 1D direction, the analogy of

165 the mass flux can be thus defined: $\rho q_x \equiv nD_x \frac{\partial C}{\partial x} - q_x C$. This connection incorporates
 166 hydrodynamic dispersion, which is inherent in chemical transport resulting in observed long
 167 tails, into the description of the partially saturated water parcels moving within the conceptual
 168 karst domain. Thus, the analogy of chemical transport and water flow is expected to show long
 169 tailing in simple flow scenarios, and was established even for pure diffusion (Cortis and
 170 Knudby, 2006).

171



172

173 **Figure 1.** Schematic illustration of (a) water parcels (blue ovals) in a karst aquifer, and (b)
 174 chemical tracer parcels (green ovals) in a porous medium (black grains) flowing through
 175 preferential pathways and accumulating in adjunct immobile regions. The resulting
 176 (schematic) measurements of the (c) temporal volumetric discharge, and (d) tracer
 177 concentration that are measured at the spring outlet further downstream.

178

179 Thus, transport equations – either advection-dispersion equations (ADE; Eq. (6)) for Fickian
 180 transport, or a CTRW formulation for non-Fickian transport (see Sect. 3.1) can be used, where
 181 the chemical tracer concentrations that these equations solve for $C(x,t)$ are conceptually
 182 identical to the relative concentration of water parcels. The concentration at a specific point is
 183 analogous to the moisture content, and the classical $C(t)$ breakthrough curve is analogous to
 184 the (volumetric) amount of water per time reaching the domain outlet (or measurement plane).

185 3 Methods

186 3.1 CTRW-PT simulations

187 In this study, a particle tracking (PT) implementation of the CTRW framework was employed
188 to devise a model capable of simulating spring discharge using the rainfall data as input. The
189 CTRW-PT model, characterized by stochastically defined particle transitions, is a Lagrangian
190 approach to solving the partial differential equations defined in the CTRW mathematical
191 framework. The movement of the particles, representing water parcels as described in the
192 ansatz (see Sect. 2), is described by equations that define the probability of particles to make
193 transitions in both space and time (Elhanati et al., 2023). For 1D cases, the transport is governed
194 by two probability density functions, $p(s)$ and $\psi(t)$, which define the particle movement in space
195 and time, respectively. An exponential form for $p(s)$ and a truncated power law (TPL) form for
196 $\psi(t)$ are used:

$$197 \quad p(s) = \lambda_s^2 \exp(-\lambda_s s) , \quad (7)$$

$$198 \quad \psi(t) = C \frac{\exp(-t/t_2)}{(1+t/t_1)^{1+\beta}} . \quad (8)$$

199 Here, λ_s^2 and C serve as normalization factors for $p(s)$ and $\psi(t)$, respectively. The TPL is
200 governed by β , the power law exponent ($0 < \beta < 2$), which is a measure of the non-Fickian
201 nature of the transport, t_1 , the characteristic transition time, and t_2 , the cutoff time to initiate
202 transition to Fickian transport. The particle velocity, v_ψ , and the generalized dispersion, D_ψ ,
203 are defined as the first and second spatial moments of the chemical species plume in the flow
204 direction (Berkowitz et al., 2006) For a 1D system:

$$205 \quad v_\psi = \frac{\bar{s}_x}{\bar{t}} = \frac{\int_0^\infty p(s)s^2 ds}{\int_0^\infty \psi(t)t dt} , \quad (9)$$

$$206 \quad D_\psi = \frac{1}{2} \frac{\bar{s}_x^2}{\bar{t}} = \frac{1}{2} \frac{\int_0^\infty p(s)s^3 ds}{\int_0^\infty \psi(t)t dt} , \quad (10)$$

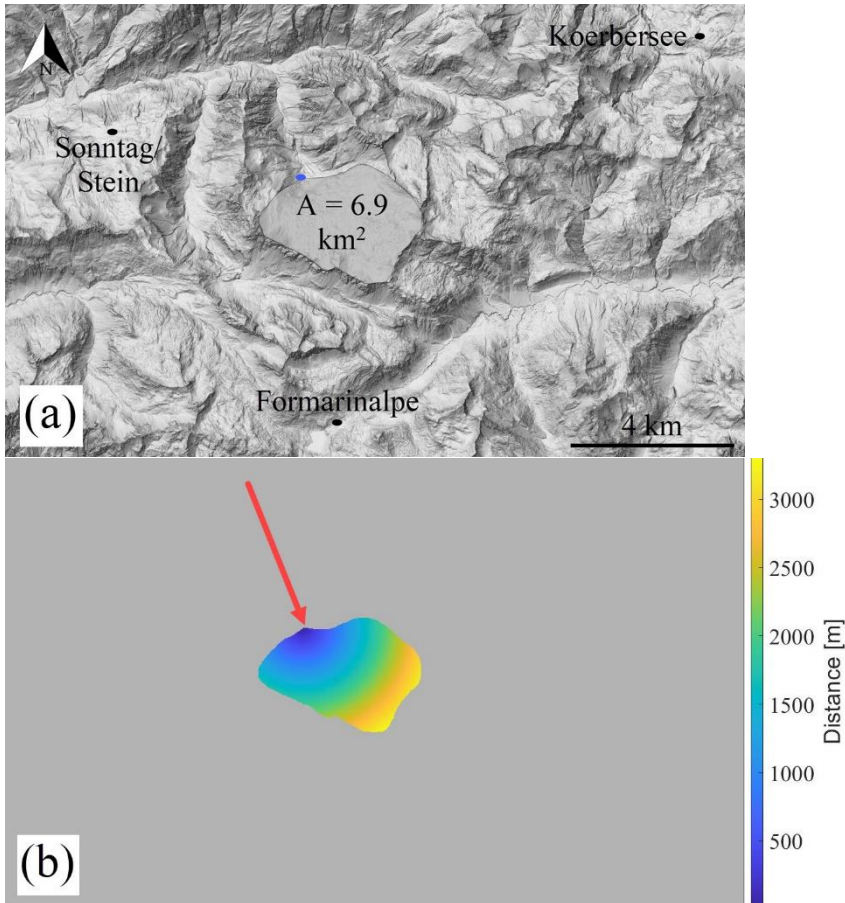
207 where \bar{s}_x and \bar{t} are the mean step size and time, respectively.

208 Inserting the probability density functions (Eqs. 7 and 8) into Eqs. 9 and 10, and defining $\tau_2 \equiv$
209 t_2/t_1 yields a mathematical relation among v_ψ , D_ψ , β , τ_2 , t_1 , t_2 and λ_s (see Nissan et al., 2017
210 for a full mathematical development). By treating the first four variables (v_ψ , D_ψ , β , τ_2) as
211 fitting parameters, the other three (t_1 , t_2 , λ_s) are immediately determined, allowing
212 optimization of the CTRW-PT model to a specific flow scenario (see Table 1).

213 The intricate three-dimensional flow field of a karst system can be conceptualized in a model
214 that considers the relationships between storage and discharge. These kinds of models, known
215 as lumped models, have been extensively used in simulation of karst systems (Hartmann et al.,
216 2014). Herein, a similar approach is applied, i.e., conceptualizing the system as a series of
217 specific physical transitions. However, in the context of the CTRW-PT model, an equivalent
218 medium to the karst system is defined in the form of a one-dimensional domain. Water is
219 introduced into the domain along its entire extent and flows to the domain outlet.

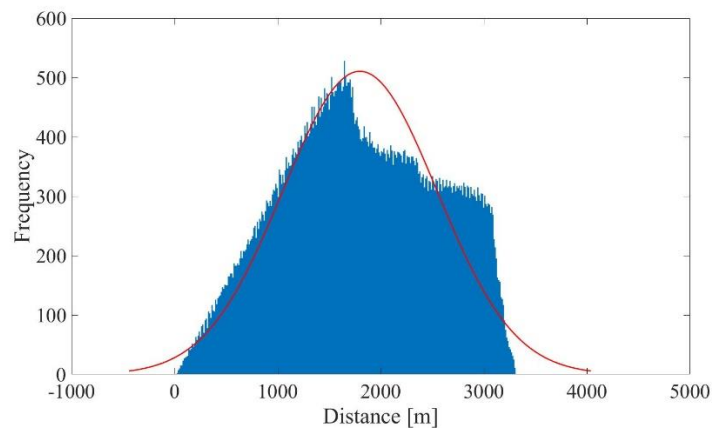
220 The 1D conceptualization is facilitated by the well-defined spatial characteristics of the system,
221 namely the catchment area and spring outlet (Fig. 2a). The distance of each point on the surface
222 of the catchment to the spring outlet is calculated (Fig. 2b), which yields a frequency histogram
223 of distances (Fig. 3). The histogram shape is dependent upon the initial image resolution and
224 the chosen bin size and yields discrete distances. To sample continuum particle entry locations
225 without dependence on bin size, a distance distribution, fitted to the histogram using MATLAB,
226 dictates how new particles are introduced into the system along the 1D domain (physically
227 unrealistic, negative sampled values are set to 0). A normal distribution was chosen as a
228 simplified representation of the distance distribution; preliminary simulation results were
229 similar for different skewed distributions. The actual underground flow path between each
230 point and the outlet spring is longer than the linear distance between the two points, as the
231 water must travel through the tortuous path through the existing conduits and fissures. The
232 distances are therefore multiplied by an empirical tortuosity factor (L), which serves as an
233 optimization parameter (see Table 1).

234



235

236 **Figure 2.** (a) Map of the Disnergschroef study area. The three weather stations in which rainfall
 237 was measured are marked with black dots, the measured spring outlet is marked with a blue
 238 dot (basemap: Land Vorarlberg – data.vorarlberg.gv.at); (b) Distances from the catchment
 239 area to the spring outlet. The distances are marked by a color scale. The spring outlet is marked
 240 by a red arrow.

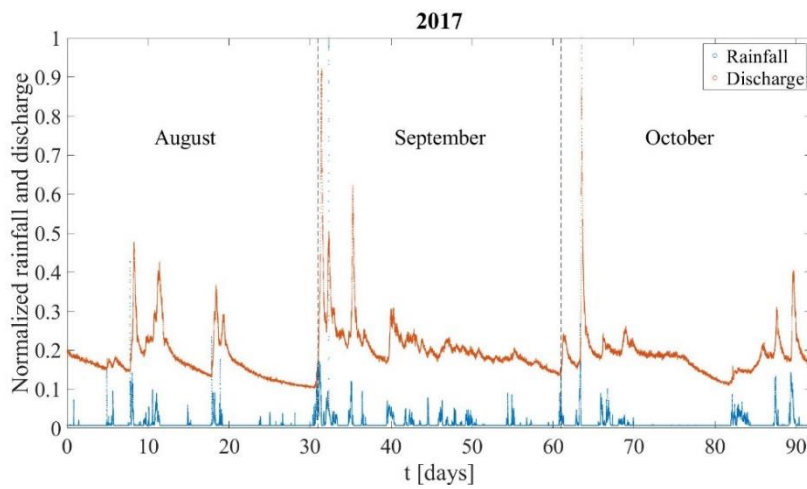
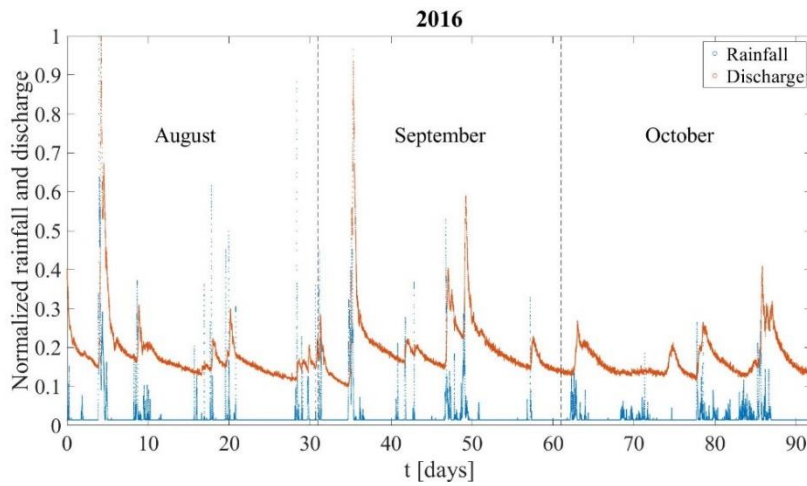


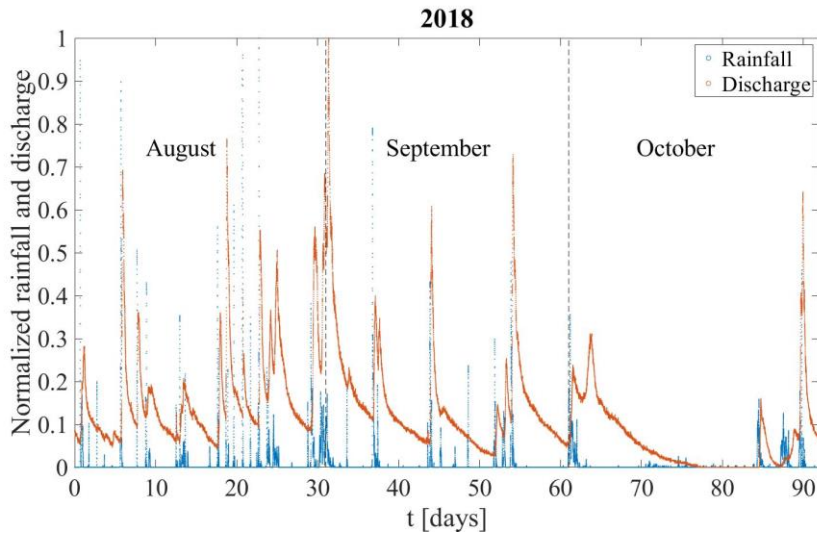
241

242 **Figure 3.** Distribution of distances from catchment area to spring outlet. The red line represents
 243 a fitted normal distribution ($\mu=1.8 \times 10^3$; $\sigma=747$).

244 Discharge at the spring is sampled every 15 minutes ($L s^{-1}$). The minimum measured discharge
245 represents the baseflow discharge. Raw rainfall data from three nearby weather stations (Fig.
246 2a) are measured in millimeters per 15 minutes. The data from the three stations are averaged,
247 and the catchment area is used to convert the data into liters per second (Fig. 4). To achieve
248 higher temporal simulation resolution, linear interpolation was used to resample the time series
249 to match a smaller simulation time step (100 s).

250





253

254 **Figure 4.** Rainfall and discharge curves for the 2016, 2017 and 2018 datasets. The data are
 255 normalized according to the maximum rainfall and discharge values, respectively, for each of
 256 the three years.

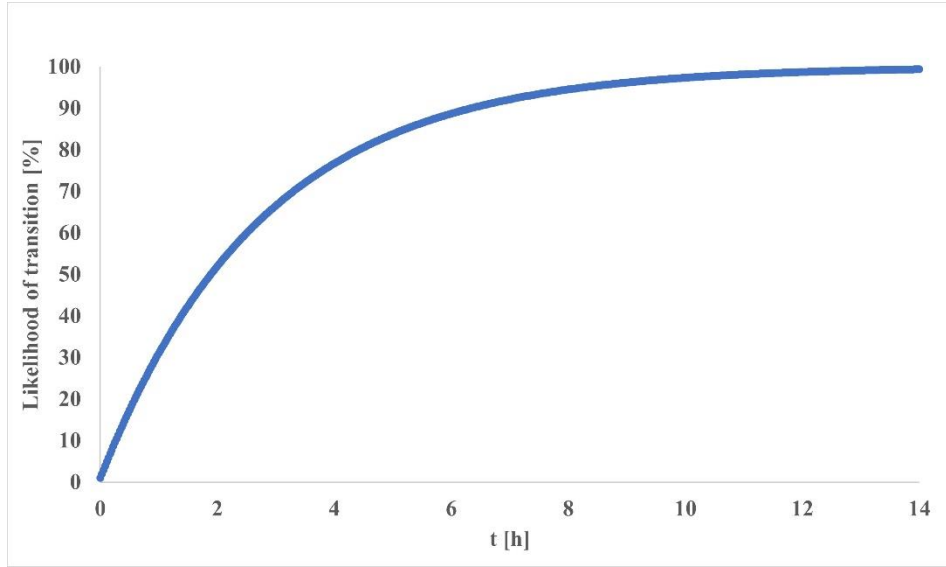
257

258 For an ideal system, in which all incoming rainwater is discharged through the spring outlet,
 259 the ratio of total rainwater to total discharge is expected to be unity. However, considering the
 260 uncertainty in the contributions of hydraulic parameters to the catchment water budget, e.g.,
 261 flow to deeper parts of the aquifer and/or other springs, and evapotranspiration, the rainfall
 262 function must be adjusted by a calculated observed recharge capacity to yield the recharge
 263 function:

264
$$recharge(t) = rainfall(t) \times \frac{\sum discharge(t) - baseflow}{\sum rainfall(t)} \quad (11)$$

265 where $rainfall(t)$ and $discharge(t)$ are the measured rainfall and discharge time series. The ratio
 266 multiplying the rainfall function is defined here as the recharge capacity parameter. The
 267 baseflow was subtracted from the total discharge for the recharge capacity calculation, to
 268 account for the background discharge not related to the spring response to rainfall. While a
 269 constant recharge capacity factor is employed in this study, due to the negligible surface runoff,
 270 it is important to note that the rainfall-to-recharge ratio may be influenced by temporal
 271 variations, rainfall intensity, and spatial characteristics. Future research should consider the
 272 sensitivity of these variables for the specific scenarios considered. In cases where there is
 273 significant variability among them, other temporal and/or spatial ratios may be applied.

274 A common procedure in lumped karst models separates the flow into slow and fast components,
275 representing the diffusive flow in the matrix and smaller fissures and the rapid flow in the
276 conduits, respectively (Hartmann et al., 2014). The CTRW-PT, as opposed to lumped models,
277 does not utilize water flow reservoirs, and operates by tracking the motion of particles that
278 represent water parcels. Therefore, the model was adapted to implement a similar approach:
279 two different sets of CTRW parameters, which govern the probability density functions for
280 particle movement (see Eqs. 7-10), are defined to represent the two flow regimes. Each particle
281 in the simulation is defined as “slow” or “fast”, and therefore obeys the corresponding set of
282 CTRW parameters (see Table 1). Newly introduced particles are divided between fast and slow
283 flow, according to a set ratio (SF_r), and they advance in space and time by their corresponding
284 set of CTRW parameters. Furthermore, each slow particle has a likelihood to transition into a
285 fast particle (SF_i) in each simulation iteration, by changing the set of CTRW parameters that
286 the particle obeys. The transition from slow to fast flow illustrates the flow of water from the
287 matrix/fissures to the conduits. While transition of fast to slow flow is also possible in karst
288 aquifers, i.e., when the pressure gradient allows water from the conduits to enter the matrix,
289 the slow to fast transition is more prominent for this site. Thus, the likelihood of transition
290 represents the net transition from slow to fast flow. When more particles transition back from
291 fast to slow flow, the transition likelihood is lower. In this context, it is important to note that
292 the CTRW-PT is a stochastic approach, in which the system parameters are represented by
293 statistical properties. The results of CTRW-PT simulations are, therefore, representative of an
294 ensemble average of many realizations. As depicted in Fig. 5, the likelihood of particle
295 transition increases rapidly, with slow particles consistently transitioning into fast particles. For
296 a transition likelihood of 0.01% and a simulation time step of 100 s, the likelihood for a single
297 particle to make a transition surpasses 99% after 458 steps which amount to 45,800 seconds
298 (~12.7 hours). In comparison, the data and simulations presented in this study span a duration
299 of 7,951,400 seconds (~92 days). These two parameters, governing the division of water
300 between fast and slow flow and the transition of water from the matrix/fissures to the conduits,
301 are pivotal in allowing the CTRW-PT model to simulate karst data.



302

303 **Figure 5.** Likelihood of particle transition from slow regime to fast regime (SF_I) as a function
 304 time for $SF_I=0.01\%$, representing a particle transition from slow matrix/fissure flow to fast
 305 conduit flow.

306

307 3.2 Model optimization and comparison to field measurements

308 Each particle represents a volume of water. The volume per particle was calculated by dividing
 309 the total observed rainfall volume by the number of simulation particles. This enables a
 310 comparison between simulated and observed recharge by volume. Given the presence of
 311 multiple model parameters, optimization is achieved by applying a bound constraint version of
 312 the MATLAB `fminsearch` function (D’Errico, 2024) to minimize the Root Mean Squared Error
 313 (RMSE) between observed and simulated discharge. A broad range of constrained parameters
 314 were investigated, as detailed in Table 1. The 2016 dataset was first used for model parameter
 315 estimation, while the 2017 and 2018 datasets served as targets for validation, by considering
 316 them for prediction using the optimized parameters from the 2016 dataset.

317 The Nash-Sutcliffe efficiency (NSE) and modified balance error (BE) were calculated for the
 318 optimized simulations, as a measure of the goodness of fit. The NSE and BE are the
 319 performance criteria utilized, for example, by the widely used KarstMod software (Frank et al.,
 320 2021). They are defined as the normalized variant of the mean squared error and the relative
 321 bias of the simulated and observed flow durations, respectively:

$$322 \quad NSE = 1 - \frac{\sum(x_s(t) - x_o(t))^2}{\sum(x_o(t) - \mu_o)^2} \quad (12)$$

323
$$BE = 1 - \left| \frac{\sum(x_o(t) - x_s(t))}{\sum x_o(t)} \right| \quad (13)$$

324 where x_s is the simulated discharge, x_o is the observed discharge and μ_o is the observed mean.
 325 The NSE performance criterion is widely used in hydrological studies and does not induce
 326 counterbalancing errors. However, it should be noted that the NSE has limitations when there
 327 is large variability in the data, and in some cases other performance criteria may be more
 328 relevant for different datasets (see Cinkus et al., 2023a for a comparison of different
 329 performance criteria).

330 4 Results and Discussion

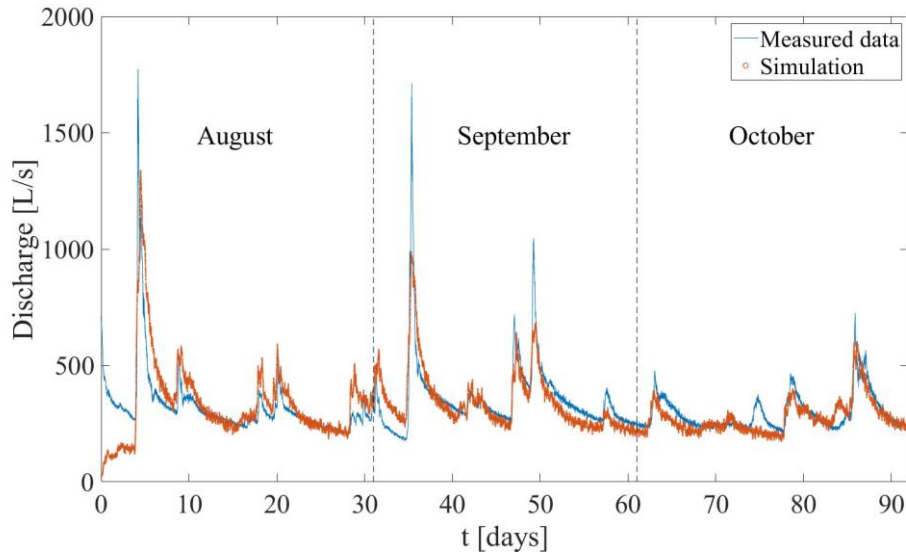
331 4.1 Optimized simulations of measured discharge

332 The optimized simulation for the 2016 dataset yields a fit (Fig. 6) that captures both the rapid
 333 response of the spring discharge to rainfall events and the protracted relaxation times
 334 characterized by the long tails evident after rainfall events. The optimized model parameters
 335 for the slow diffusive and fast conduit flow components are detailed in Table 1.

336 **Table 1.** The investigated parameter space and optimized values found.

Parameter	Minimum value	Optimized value	Maximum value	Description
v_ψ^f	10 m h ⁻¹	360 m h ⁻¹	3000 m h ⁻¹	Fast v_ψ
D_ψ^f	10 m h ⁻¹	360 m ² h ⁻¹	3000 m h ⁻¹	Fast D_ψ
β^f	1.4	1.7	2	Fast β
τ_2^f	10 ³	10 ⁶	10 ⁹	Fast τ_2
v_ψ^s	0.1 m h ⁻¹	18 m h ⁻¹	1000 m h ⁻¹	Slow v_ψ
D_ψ^s	1 x 10 ⁷ m ² h ⁻¹	3.6 x 10 ⁸ m ² h ⁻¹	1 x 10 ⁹ m ² h ⁻¹	Slow D_ψ
β^s	1	1.2	1.8	Slow β
τ_2^s	10 ⁵	10 ⁸	10 ¹¹	Slow τ_2
L	1.2	1.6	2	Tortuosity
SF_r	0	0.95	1	Slow to fast particle ratio
SF_l	0 %	0.01 %	10 %	Slow to fast particle transition likelihood

337



338

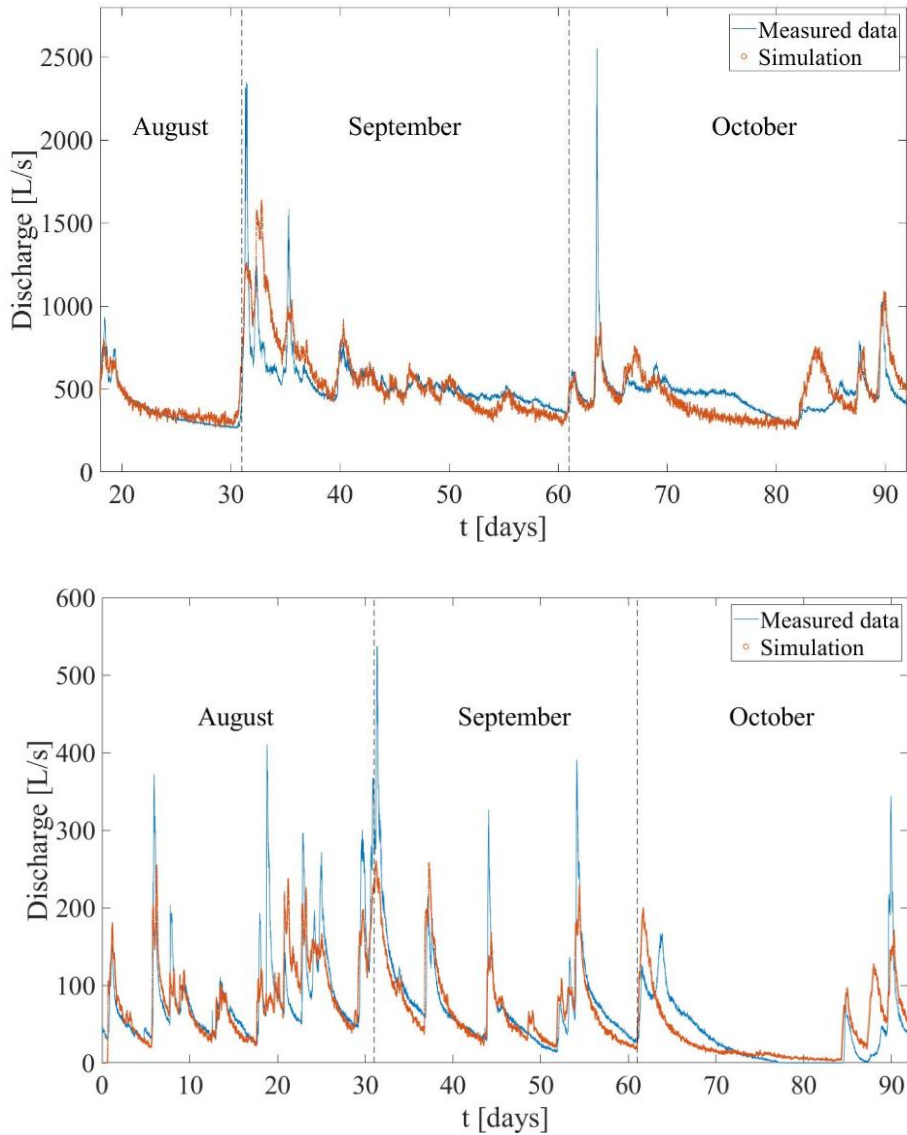
339 **Figure 6.** Measured and simulated spring discharge for the 2016 dataset ($NSE=0.5$; $BE=0.98$).

340 The differences between the fast and slow flow components, as illustrated by the respective
 341 optimized CTRW parameters, elucidate the contribution of each flow component to the
 342 volumetric discharge. The fast flow velocity parameter ($v_{\psi}^f = 360 \text{ m h}^{-1}$) is much larger than
 343 the slow flow velocity parameter ($v_{\psi}^s = 18 \text{ m h}^{-1}$) showing how incoming rain can rapidly
 344 flow to the spring outlet, when travelling through the large conduits. The slow diffusive flow,
 345 however, has a much longer travel time than the fast flow. Another clear difference between
 346 the two components which is evident from the optimized values is the degree of anomalous
 347 transport. The fast flow β (1.7) and τ_2 (10^6) parameters lead to a more symmetrical contribution
 348 to the resulting discharge around the peak following the recharge event, compared to the slow
 349 flow parameters ($\beta=1.2$, $\tau_2=10^8$), which create a long tail after the discharge peak. The slow
 350 flow is also much more dispersive ($D_{\psi}^s = 3.6 \times 10^8 \text{ m}^2 \text{ h}^{-1}$) compared to the fast flow ($D_{\psi}^f =$
 351 $36 \text{ m}^2 \text{ h}^{-1}$), which contributes further to the long discharge tails. The optimized parameters
 352 show a strong prominence of the slow flow over the fast flow: 95% of newly introduced
 353 particles are introduced as slow particles (SF_r), with a 0.01% likelihood for a slow particle to
 354 transition at each iteration to a fast regime (SF_f). The optimized tortuosity factor of 1.6 found
 355 for the Disnergschroef system is somewhat higher than that found in some cases (~ 1.2 - 1.4 , e.g.,
 356 Jouves et al., 2017; Collon et al., 2017), but well within the range (1.1-3.9) reported for karst
 357 systems (e.g., Assari and Mohammadi, 2017). The higher value can be attributed to the
 358 morphology of the specific system, and also to the fact that while tortuosity is often calculated
 359 at the cave branch scale (e.g., Jouves et al., 2017; Collon et al., 2017), the CTRW-PT model

360 uses a catchment scale tortuosity factor. The variability of tortuosity in different karst
361 morphologies should therefore be recognized when considering different modeling scenarios.

362 The fit obtained for the 2016 dataset modeling is satisfactory considering the inherent
363 uncertainty associated with the input data. The three weather stations used to measure the
364 precipitation are not located inside the catchment area, and different precipitation data were
365 measured at each station, which can be seen by examining the cross-correlation coefficients
366 between the 2016 discharge and rainfall data: 0.20, 0.22 and 0.15 for stations Koerbersee,
367 Formarinalpe, Sonntag/Stein, respectively (Fig. 2a). While an average of the three stations
368 provides an acceptable estimate of the recharge over the given time period, the variability of
369 local rain events is overlooked, which may be common in the high mountainous topography.

370 The same set of CTRW parameters optimized for the 2016 data – without further adjustment –
371 was employed to interpret the 2017 and 2018 datasets (Fig. 7). Both datasets show that the
372 simulated discharge after rainfall events predicts the onset, length and volume of the measured
373 discharge. This is especially true for the many discharge peaks exhibited by the 2018 data.



374

375 **Figure 7.** Measured and simulated spring discharge for the 2017 (top; $NSE=0.33$; $BE=0.98$)
 376 and 2018 (bottom; $NSE=0.63$; $BE=0.96$) datasets. Note that due to the large differences in
 377 maximum discharge between the three years, the vertical scales in Fig. 6 and in Fig. 7 are
 378 adjusted accordingly.

379

380 The recharge capacity parameter (applied to calculate the recharge function from the measured
 381 rainwater; see Eq. 11) was calculated as 0.43 and 0.45 for the 2016 and 2017 datasets,
 382 respectively. These values suggest that $\sim 40\%$ of the incoming rainfall reaches the outlet spring,
 383 with the remaining water reaching deeper parts of the aquifer that are less mobile. The drier
 384 2018 dataset, however, displayed a much lower value of 0.19. The variability of the recharge
 385 capacity parameter in different time periods, as a function of the rainfall pattern and amount,

386 highlights the importance of this parameter to the correct prediction of the system discharge
387 response to rainfall.

388 **4.2 Prominence of the slow flow component in the Disnerschroef system**

389 The prominence of the slow component in this karst system is evident from both the high SF_r
390 and low SF_1 . The consistency of this finding, across the three datasets (Fig. 6 and 7), agrees
391 with the analysis by Frank et al. (2021) of the recharge/discharge relationship. They observed
392 that while the flow from epikarst to conduit and matrix is highly variable and rainfall-
393 dependent, the matrix to conduit flow remains relatively constant up to a threshold. The
394 coupling of the two flow processes produces a distinctive discharge pattern characterized by a
395 sharp rapid peak after a rainfall event, followed by a long tail during recession and a return to
396 baseflow. The current analysis is similar and further emphasizes that the volumetric
397 contribution of the slow flow is substantial, particularly influencing the extended tails. In
398 contrast, the fast flow plays a more straightforward role, contributing predominantly to
399 discharge peaks by quickly expelling introduced rainwater from the system.

400 Given the importance of karst systems for human consumption, monitoring and prediction of
401 system discharge is especially important during high and low flow scenarios. These extreme
402 events can have consequences on water quality, including over-consumption during dry periods
403 and increases in turbidity and bacterial activity in high flow conditions (Pronk et al., 2006).
404 The frequency of both dry periods and heavy rainfall events has been shown to rise due to
405 climate change (Stoll et al., 2011), and this may well increase in the near future. In this context,
406 the high peaks and long tails associated with these flow conditions have proven to be the most
407 difficult to correctly predict, across different karst modeling approaches (Jeannin et al., 2021).
408 The results presented of the CTRW modeling exhibit the long tails associated with low water
409 flow. The 2018 dataset, in particular, which represents a dry summer compared to the other two
410 datasets, exemplifies the robustness of the model in predicting low flow conditions.

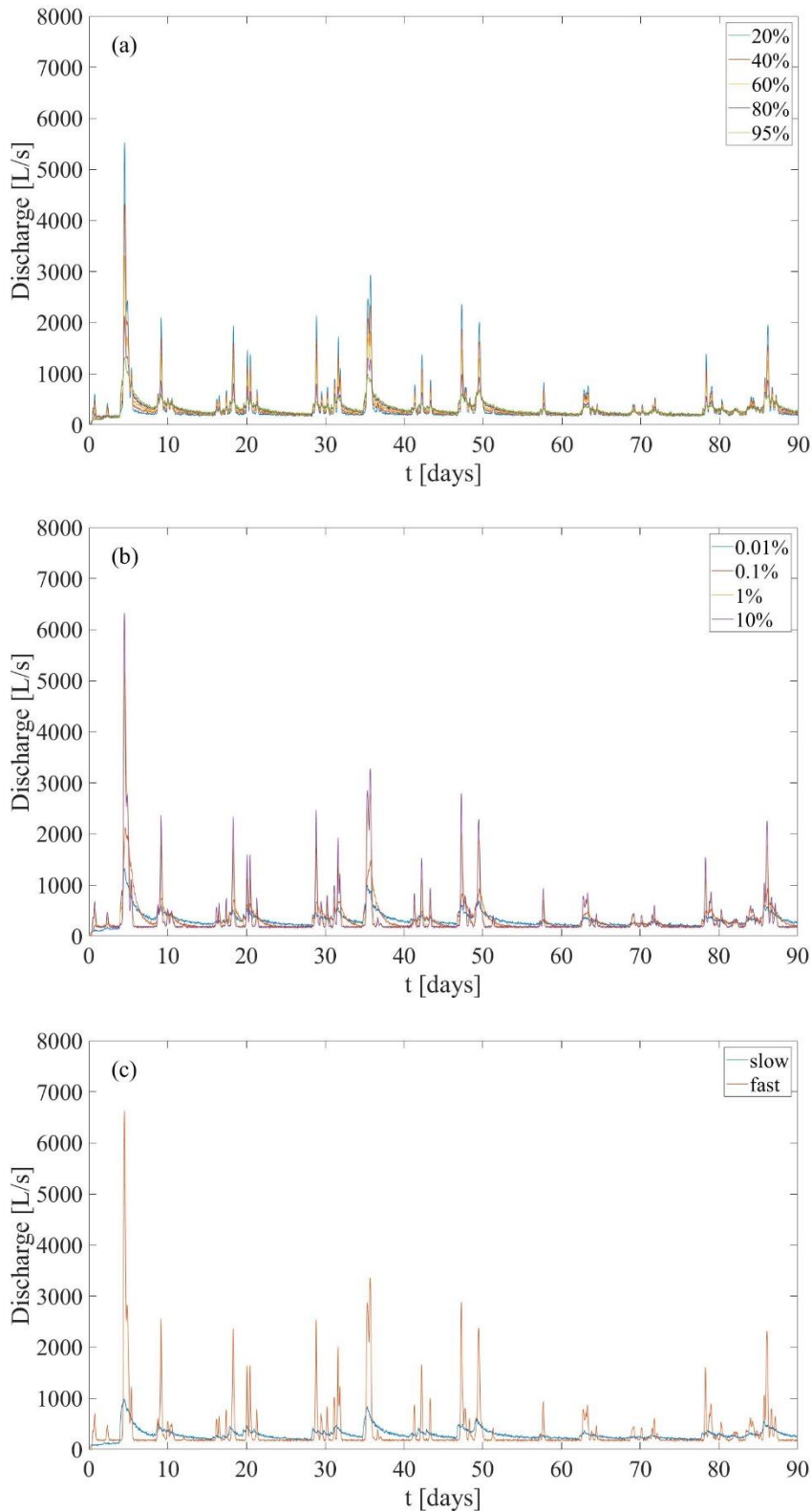
411 **4.3 The contribution of the slow and fast flow components to simulated discharge**

412 The results for all three datasets do not show agreement between the maximum simulated and
413 observed discharge values that are found immediately after high recharge events. The fast
414 response of discharge to the incoming rain in karst systems after high recharge events has been
415 described in previous studies as a piston effect (Aquilina et al., 2006; Hartmann et al., 2014).
416 Incoming rain creates a rise in discharge before the rainwater reaches the outlet, as the increase
417 in hydraulic head pushes out water that was retained in the system before the rain. This effect

418 was shown specifically in the Disnerschroef system by Frank et al. (2021) which measured a
419 2.5-hour difference between the first response of spring discharge to a rainfall event, to the
420 arrival of the rainwater to the outlet. The model herein does not explicitly take this effect into
421 account, which creates the negative bias in modeling the high peaks. While outside the scope
422 of this study, this feature might be addressed in the future by adding a third flow component,
423 or by further refining the CTRW parameters of the particles present in the system prior to the
424 rainfall event to represent the increase in flow velocity.

425 To further examine the effect of both the slow and fast flow components on the simulated
426 discharge, simulations that examine the SF_1 and SF_r parameters across a wider range were
427 conducted (Fig. 8). Simulations that contained only fast or slow particles (Fig. 8a), clearly show
428 that fast flow discharge responds very quickly to rainfall and produces no observable tails. In
429 contrast, the slow flow produces very long tails. It is noteworthy that the first response of the
430 slow flow is similar to the fast flow, as particles that are introduced to the system close to the
431 outlet have a very short length to travel to reach the outlet. Mixing of both flow regimes, either
432 by directly splitting the particles between the two regimes as they are introduced (Fig. 8b) or
433 by changing the transition likelihood (Fig. 8c) produces an intermediate response: as more of
434 the flow is slow, longer tails are found but the peaks are smaller. The SF_1 and SF_r are thus
435 important parameters as they allow application of the CTRW-PT model to different karst
436 systems. The Disnerschroef system, presented here as a case study, is characterized by a thick
437 vadose zone and negligible surface runoff. Different karst systems are likely to show different
438 SF_1 and SF_r parameters.

439



440

441 **Figure 8.** Simulation sensitivity to slow and fast particle contributions, based on the 2016
 442 rainfall data. Simulations that compare different SF_r values (a), different SF_i values (b) and
 443 only fast/slow particles (c), demonstrate the importance of the slow flow for the observed long
 444 tails in the discharge data.

445 **5 Conclusions**

446 An analogy between partially saturated water flow in karst aquifers and anomalous chemical
447 transport is established, allowing for the adaptation of the CTRW-PT model to water flow in
448 general, and for karst discharge response to rainfall specifically. The model was calibrated on
449 one summer season of measurements of spring outlet discharge response to incoming rain; it
450 was then used to predict the long tails observed in discharge measurements following rainfall
451 events in two subsequent summer seasons.

452 The investigation of the Disnerschroef karst system has shown that slow diffusive flow is a
453 predominant contributor to the volumetric discharge response to recharge events, in
454 comparison to fast conduit flow. This finding highlights the nuanced interplay between fast and
455 slow flow components in karst systems, and how they both evolve over time and as a function
456 of the recharge intensity.

457 The theoretical and practical advancements presented here offer a potentially robust tool to
458 further assess long-tailed rainfall-discharge responses in karst systems and other complex,
459 catchment-scale systems. The application of the CTRW-PT model for the Disnerschroef
460 system, specifically, has shown that it is particularly advantageous in predicting the long tails
461 observed in discharge data, compared to other modeling approaches.

462

463

464 **Data availability**

465 The data on which this article is based are available online on Zenodo:
466 <https://zenodo.org/doi/10.5281/zenodo.10635639> (Elhanati and Berkowitz, 2024).

467 **Author contribution**

468 DE, NG and BB formulated the ideas which originated the project and defined the goals and
469 aims of the study. DE developed and implemented the methodology and carried out the data
470 analysis. DE and BB drafted the initial manuscript. All authors took part in reviewing and
471 editing the final manuscript.

472 **Competing interests**

473 BB is a member of the editorial board of the journal.

474 **Acknowledgments**

475 We thank Yael Arieli for helpful insights during the practical adaptation of the CTRW-PT model
476 in the course of this study, and Simon Frank for sharing the original data sets and initial
477 background on the field measurements. The authors thank the Editor and two anonymous
478 reviewers for particularly constructive comments. DE and BB gratefully acknowledge the
479 support of the Weizmann Institute for Environmental Sustainability and the Israel Science
480 Foundation (grant No. 1008/20), respectively. BB holds the Sam Zuckerberg Professorial Chair
481 in Hydrology. NG thanks the Water Management Department of the Vorarlberg State
482 Administration for providing rainfall data.

483

484 **References**

485 Afzaal, H., Farooque, A. A., Abbas, F., Acharya, B., and Esau, T.: Groundwater estimation
486 from major physical hydrology components using artificial neural networks and deep
487 learning, *Water (Switzerland)*, 12, <https://doi.org/10.3390/w12010005>, 2020.

488 Anderson, S. and Radić, V.: Evaluation and interpretation of convolutional long short-term
489 memory networks for regional hydrological modelling, *Hydrol. Earth Syst. Sci.*, 26, 795–825,
490 <https://doi.org/10.5194/hess-26-795-2022>, 2022.

491 Aquilina, L., Ladouche, B., and Dörfliger, N.: Water storage and transfer in the epikarst of
492 karstic systems during high flow periods, *J. Hydrol.*, 327, 472–485,
493 <https://doi.org/10.1016/j.jhydrol.2005.11.054>, 2006.

494 Assari, A. and Mohammadi, Z.: Evaluation des voies d'écoulement dans un aquifère
495 karstique à partir d'essais de traçage artificiels multiples en utilisant une simulation
496 stochastique et le code MODFLOW-CFP, *Hydrogeol. J.*, 25, 1679–1702,
497 <https://doi.org/10.1007/s10040-017-1595-z>, 2017.

498 Bakalowicz, M.: Karst groundwater: A challenge for new resources, *Hydrogeol. J.*, 13, 148–
499 160, <https://doi.org/10.1007/s10040-004-0402-9>, 2005.

500 Berkowitz, B., Cortis, A., Dentz, M., and Scher, H.: Modeling non-Fickian transport in
501 geological formations as a continuous time random walk, *Rev. Geophys.*, 44, 1–49,
502 <https://doi.org/10.1029/2005RG000178>, 2006.

503 Chen, Z. and Goldscheider, N.: Modeling spatially and temporally varied hydraulic behavior
504 of a folded karst system with dominant conduit drainage at catchment scale, *Hochifen-*
505 *Gottesacker, Alps, J. Hydrol.*, 514, 41–52, <https://doi.org/10.1016/j.jhydrol.2014.04.005>,
506 2014.

507 Chen, Z., Hartmann, A., and Goldscheider, N.: A new approach to evaluate spatiotemporal
508 dynamics of controlling parameters in distributed environmental models, *Environ. Model.*
509 *Softw.*, 87, 1–16, <https://doi.org/10.1016/j.envsoft.2016.10.005>, 2017.

510 Cinkus, G., Mazzilli, N., Jourde, H., Wunsch, A., Liesch, T., Ravbar, N., Chen, Z., and
511 Goldscheider, N.: When best is the enemy of good - critical evaluation of performance
512 criteria in hydrological models, *Hydrol. Earth Syst. Sci.*, 27, 2397–2411,
513 <https://doi.org/10.5194/hess-27-2397-2023>, 2023a.

514 Cinkus, G., Wunsch, A., Mazzilli, N., Liesch, T., Chen, Z., Ravbar, N., Doummar, J.,
515 Fernández-Ortega, J., Barberá, J. A., Andreo, B., Goldscheider, N., and Jourde, H.:
516 Comparison of artificial neural networks and reservoir models for simulating karst spring
517 discharge on five test sites in the Alpine and Mediterranean regions, *Hydrol. Earth Syst. Sci.*,
518 27, 1961–1985, <https://doi.org/10.5194/hess-27-1961-2023>, 2023b.

519 Collon, P., Bernasconi, D., Vuilleumier, C., and Renard, P.: Statistical metrics for the
520 characterization of karst network geometry and topology, *Geomorphology*, 283, 122–142,
521 <https://doi.org/10.1016/j.geomorph.2017.01.034>, 2017.

522 Cortis, A. and Knudby, C.: A continuous time random walk approach to transient flow in
523 heterogeneous porous media, *Water Resour. Res.*, 42, 1–5,

524 <https://doi.org/10.1029/2006WR005227>, 2006.

525 D'Errico, J.: `fminsearchbnd`, `fminsearchcon`
526 ([https://www.mathworks.com/matlabcentral/fileexchange/8277-fminsearchbnd-](https://www.mathworks.com/matlabcentral/fileexchange/8277-fminsearchbnd-fminsearchcon)
527 `fminsearchcon`), MATLAB Central File Exchange, 2024.

528 Dentz, M., Kirchner, J. W., Zehe, E., and Berkowitz, B.: The role of anomalous transport in
529 long-term, stream water chemistry variability, *Geophys. Res. Lett.*, 50, 1–8,
530 <https://doi.org/10.1029/2023GL104207>, 2023.

531 Edery, Y., Geiger, S., and Berkowitz, B.: Structural controls on anomalous transport in
532 fractured porous rock, *Water Resour. Res.*, 52, 5634–5643, [https://doi.org/10.1111/j.1752-](https://doi.org/10.1111/j.1752-1688.1969.tb04897.x)
533 [1688.1969.tb04897.x](https://doi.org/10.1111/j.1752-1688.1969.tb04897.x), 2016.

534 Edery, Y., Guadagnini, A., Scher, H., and Berkowitz, B.: Origins of anomalous transport in
535 heterogeneous media: Structural and dynamic controls, *Water Resour. Res.*, 50, 1490–1505,
536 <https://doi.org/10.1111/j.1752-1688.1969.tb04897.x>, 2014.

537 Elhanati, D. and Berkowitz, B.: CTRW simulations of karst aquifer discharge response to
538 rainfall [Data Set], Zenodo, <https://doi.org/10.5281/zenodo.10635640>, 2024.

539 Elhanati, D., Dror, I., and Berkowitz, B.: Impact of time-dependent velocity fields on the
540 continuum-scale transport of conservative chemicals, *Water Resour. Res.*, 59, 1–19,
541 <https://doi.org/10.1029/2023WR035266>, 2023.

542 Fleury, P., Ladouche, B., Conroux, Y., Jourde, H., and Dörfliger, N.: Modelling the
543 hydrologic functions of a karst aquifer under active water management - The Lez spring, *J.*
544 *Hydrol.*, 365, 235–243, <https://doi.org/10.1016/j.jhydrol.2008.11.037>, 2009.

545 Ford, D. and Williams, P.: *Karst Hydrogeology and Geomorphology*, 1–562 pp.,
546 <https://doi.org/10.1002/9781118684986>, 2007.

547 Frank, S., Goeppert, N., and Goldscheider, N.: Improved understanding of dynamic water and
548 mass budgets of high-alpine karst systems obtained from studying a well-defined catchment
549 area, *Hydrol. Process.*, 35, 1–15, <https://doi.org/10.1002/hyp.14033>, 2021.

550 Goeppert, N., Goldscheider, N., and Berkowitz, B.: Experimental and modeling evidence of
551 kilometer-scale anomalous tracer transport in an alpine karst aquifer, *Water Res.*, 178,
552 [115755](https://doi.org/10.1016/j.watres.2020.115755), <https://doi.org/10.1016/j.watres.2020.115755>, 2020.

553 Hartmann, A., Goldscheider, N., Wagner, T., Lange, J., and Weiler, M.: Karst water
554 resources in a changing world: Review of hydrological modeling approaches, *Rev. Geophys.*,
555 52, 218–242, <https://doi.org/10.1002/2013RG000443>, 2014.

556 Jeannin, P. Y., Artigue, G., Butscher, C., Chang, Y., Charlier, J. B., Duran, L., Gill, L.,
557 Hartmann, A., Johannet, A., Jourde, H., Kavousi, A., Liesch, T., Liu, Y., Lüthi, M., Malard,
558 A., Mazzilli, N., Pardo-Igúzquiza, E., Thiéry, D., Reimann, T., Schuler, P., Wöhling, T., and
559 Wunsch, A.: Karst modelling challenge 1: Results of hydrological modelling, *J. Hydrol.*, 600,
560 <https://doi.org/10.1016/j.jhydrol.2021.126508>, 2021.

561 Jouves, J., Viseur, S., Arfib, B., Baudement, C., Camus, H., Collon, P., and Guglielmi, Y.:
562 Speleogenesis, geometry, and topology of caves: A quantitative study of 3D karst conduits,
563 *Geomorphology*, 298, 86–106, <https://doi.org/10.1016/j.geomorph.2017.09.019>, 2017.

564 Jukić, D. and Denić-Jukić, V.: Groundwater balance estimation in karst by using a conceptual
565 rainfall-runoff model, *J. Hydrol.*, 373, 302–315,
566 <https://doi.org/10.1016/j.jhydrol.2009.04.035>, 2009.

567 Kaufmann, G. and Turk, J.: Modelling flow of subterranean Pivka river in Postojnska jama ,
568 *Slovenia Modeliranje toka podzemeljske Pivke v Postojnski*, 57–70, 2016.

569 Kratzert, F., Klotz, D., Brenner, C., Schulz, K., and Herrnegger, M.: Rainfall-runoff
570 modelling using Long Short-Term Memory (LSTM) networks, *Hydrol. Earth Syst. Sci.*, 22,
571 6005–6022, <https://doi.org/10.5194/hess-22-6005-2018>, 2018.

572 Mazzilli, N., Guinot, V., Jourde, H., Lecoq, N., Labat, D., Arfib, B., Baudement, C.,
573 Danquigny, C., Dal Soglio, L., and Bertin, D.: KarstMod: A modelling platform for rainfall -
574 discharge analysis and modelling dedicated to karst systems, *Environ. Model. Softw.*, 122,
575 <https://doi.org/10.1016/j.envsoft.2017.03.015>, 2019.

576 Nissan, A., Dror, I., and Berkowitz, B.: Time-dependent velocity-field controls on anomalous
577 chemical transport in porous media, *Water Resour. Res.*, 53, 3760–3769,
578 <https://doi.org/10.1111/j.1752-1688.1969.tb04897.x>, 2017.

579 Pronk, M., Goldscheider, N., and Zopfi, J.: Dynamics and interaction of organic carbon,
580 turbidity and bacteria in a karst aquifer system, *Hydrogeol. J.*, 14, 473–484,
581 <https://doi.org/10.1007/s10040-005-0454-5>, 2006.

582 Renard, P. and Bertrand, C.: EuroKarst 2016, Neuchâtel, *Advances in the Hydrogeology of*

583 Karst and Carbonate Reservoirs, 217–229 pp., 2017.

584 Rimmer, A. and Salinger, Y.: Modelling precipitation-streamflow processes in karst basin:
585 The case of the Jordan River sources, Israel, *J. Hydrol.*, 331, 524–542,
586 <https://doi.org/10.1016/j.jhydrol.2006.06.003>, 2006.

587 Stevanović, Z.: Karst waters in potable water supply: a global scale overview, *Environ. Earth*
588 *Sci.*, 78, 1–12, <https://doi.org/10.1007/s12665-019-8670-9>, 2019.

589 Stoll, S., Hendricks Franssen, H. J., Butts, M., and Kinzelbach, W.: Analysis of the impact of
590 climate change on groundwater related hydrological fluxes: A multi-model approach
591 including different downscaling methods, *Hydrol. Earth Syst. Sci.*, 15, 21–38,
592 <https://doi.org/10.5194/hess-15-21-2011>, 2011.

593 Tritz, S., Guinot, V., and Jourde, H.: Modelling the behaviour of a karst system catchment
594 using non-linear hysteretic conceptual model, *J. Hydrol.*, 397, 250–262,
595 <https://doi.org/10.1016/j.jhydrol.2010.12.001>, 2011.

596 Wunsch, A., Liesch, T., Cinkus, G., Ravbar, N., Chen, Z., Mazzilli, N., Jourde, H., and
597 Goldscheider, N.: Karst spring discharge modeling based on deep learning using spatially
598 distributed input data, *Hydrol. Earth Syst. Sci.*, 26, 2405–2430, [https://doi.org/10.5194/hess-](https://doi.org/10.5194/hess-26-2405-2022)
599 [26-2405-2022](https://doi.org/10.5194/hess-26-2405-2022), 2022.

600 Zhang, X., Huang, Z., Lei, Q., Yao, J., Gong, L., Sun, S., and Li, Y.: Connectivity,
601 permeability and flow channelization in fractured karst reservoirs: A numerical investigation
602 based on a two-dimensional discrete fracture-cave network model, *Adv. Water Resour.*, 161,
603 104142, <https://doi.org/10.1016/j.advwatres.2022.104142>, 2022.

604